Pixelated Detector With Photon Address Event Driven Time Stamping and Correlation

George M. Williams, Jehyuk Rhee, Adam Lee, and Stephen D. Kevan

***Abstract*—We present the design, manufacture, and test results of an asynchronous event-driven address time-stamped (EDATS) pixelated array detector, operational over correlation time spans ranging from less than 10^{-6} to greater than 10^{4} s. The pixelated EDATS detector was designed to measure the equilibrium density fluctuations on a nanometer-length scale using small angle X-ray scattering in X-ray photon correlation spectroscopy (XPCS) experiments. The detector sensor chip assembly (SCA) includes a custom readout integrated circuit (ROIC), hybridized to a silicon photodiode array, optimized for 500 to 2000 eV X-ray photons. The detector is shown to be capable of handling X-ray photon event rates of 100 million X-ray events per second, with less than 85 ns timing jitter per event.**

***Index Terms*—Autocorrelation, high resolution, single photon detection, X-ray photon correlation spectroscopy, XPCS.**

I. Introduction

THE effects of weak forces manifest macroscopically when working in nanometer-length scales. The energetic interactions that arise from these forces determine the thermodynamic and mechanical properties of the material. This leads to unusual and useful material properties. These statements apply as much to superconductors and ferromagnets as they do to complex fluids and biological materials. Yet, despite the many spectacular advances made in developing new microscopy, spectroscopy, and scattering techniques, in many cases, a mechanistic understanding of the connection of materials across the microscopic–macroscopic scale continuum has yet to be achieved. Part of the reason for this is that most analysis techniques do not provide simultaneous spatial information and dynamical properties at the requisite length and time scales.

Of the available measurement techniques, photon-correlated spectroscopy (PCS), performed using coherent visible light, has been used to study small scattering wave vectors ($q < 4 \times 10^{-3}$ A^{-1}). Now, X-ray sources exist that can be used to study the space–time correlations in disordered systems at the nanoscopic- and atomic-length scales of materials not absorbing visible light. Using the latest brilliant synchrotron X-ray sources, inelastic scattering of X-rays can be used to probe the dynamic properties of matter at frequencies from 10^{14} Hz down to approximately 10^{8} Hz, to achieve scattering wave vectors from 10^{-2} A^{-1} to 10 A^{-1}.

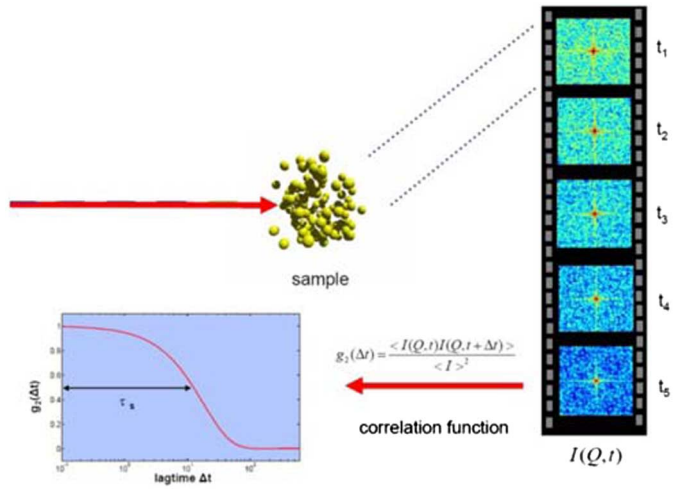

Fig. 1. XPCS allows the dynamic structure factor [$S(Q,t)$, where Q is the scattering vector and t is time] to be determined on short length scales in the time domain.

Looking forward, as brighter, free-electron laser and storage ring X-ray sources become available, X-ray photon correlation spectroscopy (XPCS), which is based upon the scattering of transversely coherent beams of X-rays [1]–[8] (e.g., see [9]–[11]), holds the promise of giving greater insight into the dynamical phenomena of condensed matter (Fig. 1). To extract information about the dynamics of the complete structure of a sample, with atomic resolution, XPCS uses fluctuations in X-ray-scattered intensity and provides information on the scale of 10^{8} Hz down to 10^{-2} Hz and in the 10^{3} A^{-1} to 10^{0} A^{-1} length scale. The direct temporal measurements by XPCS can then be used to analyze low-frequency dynamics and to provide an alternative view that can help in understanding processes with time-varying dynamics.

The feasibility of XPCS at these scales has now been demonstrated in applications from many different fields, including studies of soft matter, hard matter, surfaces, and interfaces, including pioneering studies of dilute colloidal suspensions of gold particles [8], fractal aggregates composed of small palladium particles [12], and freely suspended liquid crystal films [3].

Manuscript received November 27, 2013; revised February 18, 2014; accepted April 09, 2014. Date of publication July 31, 2014; date of current version August 14, 2014. This work was performed under Department of Energy (DOE) contract DE-SC0002430. The work of S. D. Kevan was supported by the U.S. Department of Energy, Office of Basic Energy Sciences, Division of Materials Science and Engineeringunder grant number DE-FG02-11ER46831.

G. M. Williams, J. Rhee, and A. Lee are with Voxtel, Incorporated, Beaverton, OR 97006 USA (e-mail georgew@voxtel-inc.com).

S. D. Kevan is with the Department of Physics, University of Oregon, Eugene, OR 97403 USA (e-mail kevan@uoregon.edu).

Color versions of one or more of the figures in this paper are available online at http://ieeexplore.ieee.org.

Digital Object Identifier 10.1109/TNS.2014.2327513

While XPCS has achieved some maturity, the method is much more challenging than those that use lasers. First, in XPCS, it is necessary to use a partially coherent X-ray beam, which contains far fewer photons than a laser beam. Second, the cross section in X-ray scattering is far smaller than in light scattering. When the coherent X-rays are scattered from a disordered sample, the diffraction pattern has a grainy appearance known as speckle.

Individual speckles fluctuate in relation to the dynamics of the sample at a length scale of $2\pi/Q$, where Q is the scattering vector. The speckle scattering pattern $I(Q,t)$ is then autocorrelated with respect to time t. The resultant intensity–intensity autocorrelation function $g_2(Q,t)$ is related to the intermediate scattering function of the sample via [13]

$$g_2(Q,t) = \frac{\langle I(Q,t)I(Q,t+\tau)\rangle_\tau}{\langle I(Q,t)\rangle_\tau^2} = 1+\beta[f(Q,t)]^2 \quad (1)$$

where β is the optical speckle contrast, $f[Q,t] = S[Q,t]/S[Q]$ is the normalized intermediate scattering function, τ is the time delay, and $S[Q] = S[Q,0]$ is the static structure factor.

XPCS science was first conducted using single-channel detectors. To acquire data from many coherent areas (speckles) simultaneously, two-dimensional (2D) area detectors were first demonstrated several years ago using charge-coupled devices (CCDs) consisting of approximately 10^6 pixels, [14]. These area arrays increased experiment efficiency by several orders of magnitude compared to single-channel detectors. In multispeckle XPCS, where many speckles are recorded simultaneously, the entire frame of an area detector is read out at high speed, which greatly improves the signal-to-noise ratio (SNR) relative to a point-detector setup, which can only probe a few speckles at a time.

Jakeman [15] has developed an SNR model for an XPCS experiment, adapted for CCD arrays, which is valid at low count rates. In its simplest form, the expression reads:

$$\mathrm{SNR_{CCD}} = \beta I\sqrt{T\tau_\mathrm{a}}\eta\sqrt{\tau_\mathrm{a}/(\tau_\mathrm{a}+\tau_\mathrm{t})}\sqrt{n_x n_y} \quad (2)$$

where β is the speckle contrast, I is the intensity per pixel, η is the quantum efficiency, T is the total measurement time, τ_a is the accumulation time per frame, τ_t is the readout time of the detector), and $n_x n_y$ is the number of pixels in the region of analysis.

However, currently available 2D detectors, including both fast-framing direct-detection CCDs or scintillator-coupled CCDs, cannot provide frame rates considerably greater than 10 to 100 Hz, due to the required detector readout times, which limits the time resolution and dynamic range of XPCS experiments. Furthermore, the processing tasks required to perform autocorrelation on a full array creates a bottleneck for XPCS experiments. These bottlenecks have been addressed in recent CMOS imaging technologies [16]–[18].

II. Technical Approach

A. EDATS Detector Architecture

To provide the increased X-ray speckle SNR contrast, timing resolution, and pixel density required for XPCS experiments, while minimizing the data bandwidths associated with fast framing cameras [13], [19], we developed an event-driven address time-stamp (EDATS) X-ray photon counting (XPC) pixelated array detector (PAD) with timing performance shown in Fig. 2. The detector requires only simple control and processing electronics to generate a low-bandwidth, purely digital interface, which can be used to conduct real-time spatial/temporal data correlation processing. EDATS specifications are provided in Table I.

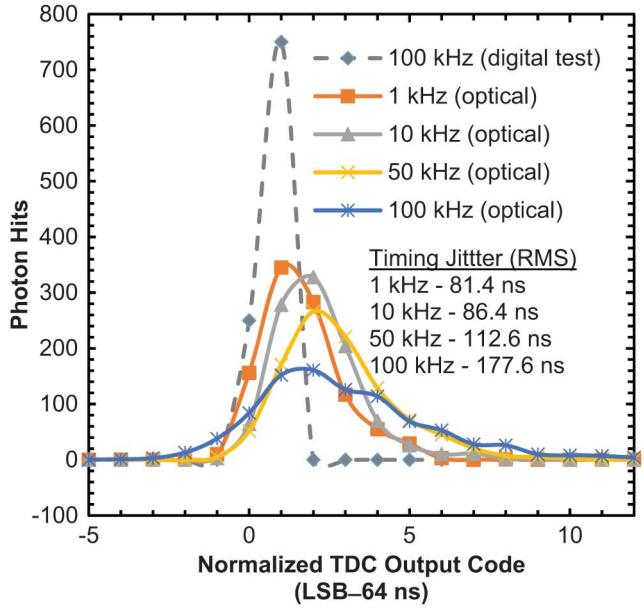

Fig. 2. Measured timing performance of EDATS XPC sensor. The RMS timing jitter is 81.4 ns RMS with a 1 kHz pixel rate and a 64 ns TDC resolution.

TABLE I
EDATS-XPC Sensor Focal Plane Specifications

Sensor Parameter	Units	Specification
Spatial Resolution	pixels	492 x 492
Area	mm	21.6 x 21.6
Pixel pitch	µm	40
X-ray energy	keV	0.5–2.0
Detector thickness	µm	20
Read noise	e- (RMS)	16
Threshold dispersion	e- (RMS)	17
Timing resolution	ns (RMS)	85
Sensor count rate	photons/sec	$100*10^6$
Power consumption	watts	3
CMOS process		TSMC 0.25 µm

The EDATS detector (Fig. 3) is based on a sensor-chip assembly (SCA), composed of a custom-designed 492×492-element pixelated CMOS readout integrated circuit (ROIC), the Voxtel model VX-807 ROIC, flip-chip-solder-bonded to an array of silicon (Si) PIN photodiodes (PDs) with a $40\text{-}\mu\mathrm{m} \times 40\text{-}\mu\mathrm{m}$ pixel pitch. The fully depleted $20\text{-}\mu$m-thick Si pixelated detector layer, fabricated on 4000 Ω-cm float zone silicon (n-), is optimized for absorbing 0.5 to 2 keV X-ray photons.

The VX-807 ROIC is designed with an asynchronous EDATS readout architecture. The X-ray photons are first converted to signal carriers in the Si photodetectors, and the charge carriers are converted to a voltage signal in the amplification circuits of

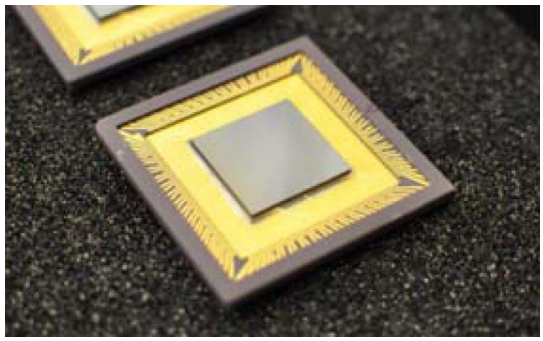

Fig. 3. Picture of a 492×492 element EDATS-XPC sensor. The Si detector array has been hybridized to the VX-807 ROIC design and packaged in a ceramic PGA.

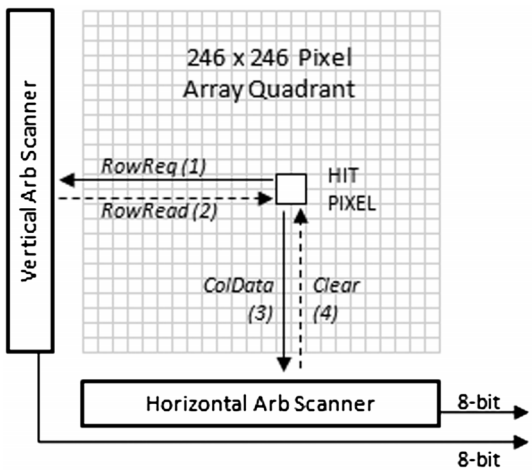

Fig. 4. Top-level block diagram of EDATS arbitration readout for a single quadrant, showing the digital control signal of the event address arbitration logic to and from the pixel, which are annotated in order of operation following photon detection.

each pixel of the VX-807 ROIC. When the X-ray-photon-generated voltage signal in a pixel exceeds a user-programmable threshold voltage level, pixel circuits set a flag, which is then broadcast to address arbitration circuits located at the periphery of the X-ray-sensitive portion of the array (see Fig. 4). The arbitration circuits are used to determine the (x, y) address of the incident X-ray event and to reset the pixel circuits so that they are again ready to detect X-ray photons. The event-driven addresses of the pixels hit by the incident X-ray photon are transmitted off chip to a time-to-digital processor, where they can be time-stamped with better than 85 ns accuracy. To increase count rate, the VX-807 ROIC is divided into four quadrants. As shown in Fig. 5, each quadrant has individually operated address arbitration circuits, which allows for a maximum photon count rate of about 10^8 counts per second per array.

These circuits make the EDATS detector capable of asynchronous acquisition of X-ray photon location and arrival time, at modest photon flux rates, without in-pixel signal or amplitude time storage or full-frame readout. By eliminating the need for full-frame readout, in the EDATS array, dead time is minimized and data rates are dramatically reduced relative to fast framing detector approaches, which improves the SNR.

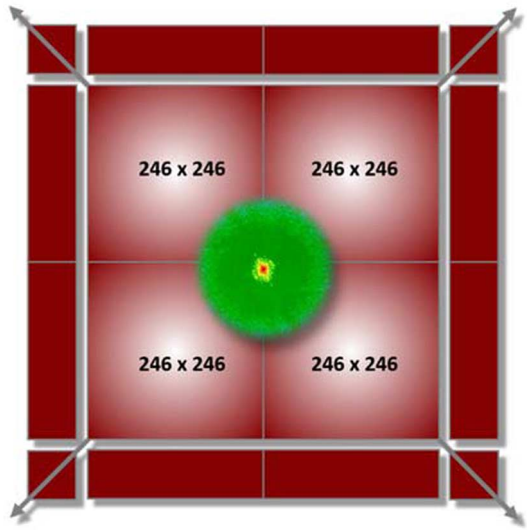

Fig. 5. EDATS-XPC sensor pixelated array detector. Shown is the four-quadrant architecture, where each quadrant of the design acts independently of the other three quadrants. Arrows represent an LVDS bus that broadcasts the 18-bit (8-bit x, 8-bit y, and 2-bit quadrant) address of the X-ray photon event to an external TDC with better than 85 ns accuracy.

Assuming an interphoton arrival time significantly larger than the maximum pixel reset time of 85 ns, the photon-counting rate given by (2) reduces to

$$\text{SNR} \approx \beta I \eta \sqrt{T}. \tag{3}$$

Since the speckle size is given by $\sigma = (\lambda d)/a$, where λ is the wavelength, d is the distance between sample and detector, and a is the illuminated area, the speckle contrast β can be approximated by $\beta = 1/[1 + (P/\sigma^2)^2]$, where P is the pixel area (40×40 μm^2 for EDATS).

B. VX-807 ROIC

The VX-807 ROIC is a 492×492 unit cell array of circuits optimized for detecting the spatial and time of arrival of incident X-ray photons.

1) Pixel Design—Analog Front End: Analog front-end (AFE) circuits of each pixel of the VX-807 ROIC, shown in Fig. 6, are designed for low-noise operation, with the goal of being able to detect X-rays at the oxygen K-edge at around 530 eV. Assuming that, when the detector absorbs a 530 eV X-ray, it responds by generating 0.274 electrons per eV, and that an SNR of 6 will provide a suitably low false-positive rate, pixel circuits with a read noise of approximately 20 e$^-$ RMS are required (see Table II).

In-pixel AFE circuits of the VX-807 ROIC capable of such low-noise performance include a two-stage amplifier consisting of a capacitive transimpedance amplifier (CTIA) followed by a differentiating pulse-shaping circuit (shaping amplifier, or *shaper*), which, together, convert the signal pulse to a voltage pulse. To reduce pixel area, both the CTIA and shaper are implemented as single-ended cascode amplifiers.

After an X-ray photon is absorbed in the Si detector, the generated holes are swept to the anode contacts of the pixilated detector by the electric fields of the photodiodes. When the holes

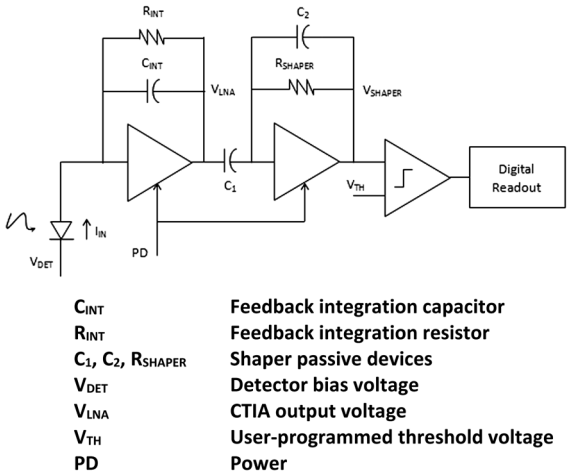

Fig. 6. Block diagram of the VX-807 ROIC pixel design showing a two-stage amplifier, consisting of a CTIA, followed by a shaping resistive transimpedance amplifier. The output pulse from the analog front end is shown to be compared to a user-defined threshold voltage. When the signal voltage pulse exceeds the threshold setting, the comparator signals to address arbitration circuits at the periphery of the photon active area.

TABLE II
NOISE AND SNR ANALYSIS OF EDATS-XPC SENSOR DESIGN

Noise Source[a]	Type	Input-referred Noise
CMOS Amplifiers	Thermal & Flicker	15.5 e^-
Discriminator Offset	FPN	11.7 e^-
AFE Gain Variation	FPN	11.2 e^-
Detector (530 eV Photon)	Shot	12.0 e^-
Total Noise		25.4 e^-
SNR (530 eV Photon)		5.71

reach the photodiode anode, they charge the front end of the amplifier, increasing the voltage at the input to the CTIA. The CTIA responds by decreasing its output voltage, forcing the photodiode current to flow through the feedback capacitance $C_{\rm INT}$. This causes the output of the CTIA to change proportionally to the integrated value of the input charge. To set the quiescent operating point of the CTIA, a large feedback resistor $R_{\rm INT}$ value is used. $R_{\rm INT}$ is chosen to be small enough to sink the dc dark current of the detector and large enough to not affect the integration of the X-ray-photon-generated signals. The CTIA reset noise and detector dark current noise are partially mitigated by the continual dc reset that takes place through $R_{\rm INT}$.

In the second stage, the C-RC shaper differentiates the CTIA output voltage, reconstructing the current pulse shape as a voltage pulse at its output. The amplitude, shape, and width of the output pulse are functions of the transfer function of the shaper. The transfer function is engineered by selection of capacitor (C_1, C_2, and C_L) and resistor ($R_{\rm SHAPER}$) components (see Fig. 6). These passive components of the shaper are chosen so as to band-limit the CTIA, filtering noise by removing the low-frequency $1/F$ noise and high-frequency thermal noise of the CTIA. To match the minimum autocorrelation time required by the XPCS experiments, the bandwidth of the AFE in-pixel circuit of the EDATS-XPC sensor is set to allow an interphoton arrival time of about 1 μs.

The resulting noise of the AFE amplification circuits is dominated by transient noise sources and fixed pattern noise (FPN). Assuming that the AFE amplifiers have a single dominant pole located at the output node, the input-referred RMS noise of the VX-807 ROIC pixel circuits can thus be approximated as

$$\mathrm{ENC}[\mathrm{e}^-] \approx \sqrt{\frac{4kT\,(2/3)\,C_{\rm INT}(C_{\rm INT}+C_{\rm DET})^2}{q^2\left[C_{\rm L}\,(C_{\rm INT}+C_{\rm DET})+C_{\rm INT}C_{\rm DET}\right]}} \quad (4)$$

where T is the operating temperature, k is Bolzmann's constant with a value of 1.380650×10^{-23} joules per kelvin (K), $C_{\rm DET}$ is detector self-capacitance and any parasitic capacitance on the CTIA input node, $C_{\rm INT}$ is feedback integration capacitance, q is the charge of an electron ($q = 1.602176487 \times 10^{-19}$ Coulombs), and C_L is load capacitance at the output of the CTIA.

This analysis considers only thermal noise sources. This is a reasonable approximation for this architecture because most $1/F$ noise components are removed by bandpass filtering with the shaper. If we assume that C_L is greater than $C_{\rm INT}$, and we substitute into (4) the CTIA transconductance g_m and closed-loop bandwidth BW in radians, then

$$\mathrm{ENC}[\mathrm{e}^-] \approx \sqrt{\frac{4kT\,(2/3)\,(C_{\rm INT}+C_{\rm DET})^2\mathrm{BW}}{q^2 g_{\rm m}}}. \quad (5)$$

To reduce input-referred noise of the read chain, (5) shows that, within the constraint of the measurement requirements $C_{\rm INT}$, $C_{\rm DET}$, and BW must be minimized, and the input g_m must be maximized. In a single-stage CTIA, bandwidth is proportional to input transconductance. As a result, the input-referred noise of the CTIA is independent of transconductance. However, as the limiting bandwidth of the VX-807 ROIC in-pixel AFE circuits is set by the shaper instead of the CTIA pole, an increase in g_m is used to reduce the detector's input-referred noise.

We implemented the VX-807 ROIC, CTIA with $C_{\rm INT}$ of 8.3 fF, which produces a CTIA conversion gain of 19.3 μV/e^-. Passive components of the shaper are $C_1 = 845$ fF and $C_2 = 12.5$ fF. The shaper feedback resistance $R_{\rm SHAPER}$ is implemented using a field-effect transistor (FET) operating in linear mode, which can be adjusted by varying the gate voltage. In this way, the gain and bandwidth of the transform function of the shaper can be tuned.

AC noise simulations were used to determine total temporal noise of 15.5 e^- RMS for the VX-807 ROIC pixel AFE circuits, which includes both thermal and flicker noise sources. As expected, AFE circuit noise is dominated by the thermal noise of the CTIA input, which contributes more than 70% of the total circuit noise.

To determine detector performance, FPN must also be taken into consideration. FPN has contributions from discriminator offset values and AFE gain variations, which contribute 11.7 e^- and 11.2 e^-, respectively. Assuming minimum X-ray photon energy of 530 eV (the oxygen K-edge), an average of 145 e^- of signal is generated in each silicon photodiode, with a corresponding shot noise of about 12.0 e^- RMS.

Table II summarizes these noise sources and shows that the SNR of the minimum X-ray photon energy for the 530 eV oxygen K-edge is predicted to be about 5.71, sufficiently high to allow for efficient threshold discrimination of photon events with low false alarm rates.

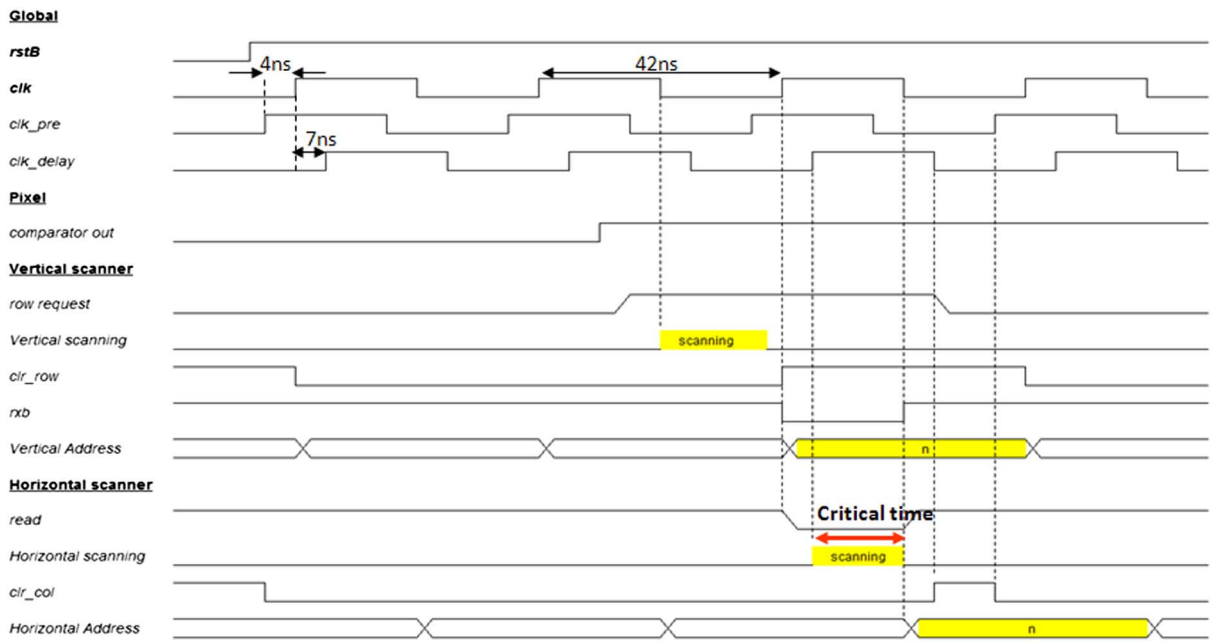

Fig. 7. Timing diagram of EDATS-XPC sensor architecture showing the critical timing constraint on maximum clock speed.

2) Pixel Design—Discriminator: To maintain sensitivity to the minimum photon energy while avoiding false triggering due to noise, the globally distributed threshold level must be set sufficiently high (i.e., greater than 3σ above the noise floor, σ). As shown in Fig. 6, in each unit cell of the VX-807 ROIC, the output of the AFE circuits drives a programmable three-stage threshold discriminator. To reduce pixel sensitivity to noise on the falling edge of the shaper output, the discriminator design is implemented with 29.4 mV of hysteresis. When an X-ray event generates a signal in the AFE that exceeds the globally distributed comparator threshold voltage level, a digital pulse is broadcast from the pixel to the address arbitration readout logic at the periphery of the array (Fig. 4).

The EDATS-XPC sensor is designed to support XPCS experiments with about 1-μs correlation timing. Thus, for a fixed threshold voltage setting, the jitter on the time stamp, including any amplitude-dependent variations in the time stamp that result from the magnitude of the pulses generated by the variety of energetic X-ray photons, must be considerably less than 1 μs. In the EDATS-XPC sensor ROIC, timing errors result from both the systematic jitter resulting from the variability in the time it takes the arbitration circuits to determine the pixel address of pulse origin, and the jitter resulting from the AFE and discriminator in the pixel.

3) Address Event-Driven Readout Logic: The VX-807 ROIC scanner circuits, located at the periphery of the photon-sensitive array, are in a digital readout block divided into three sections (see Fig. 4): 1) vertical arbitration scanner; 2) horizontal arbitration scanner; and 3) in-pixel digital readout logic. The vertical scanner polls the array and controls the selection of rows for readout. The horizontal scanner determines which pixel or pixels within the selected row captured the incident X-ray photon event.

The ROIC readout logic recovers the 16-bit address (8-bit vertical and 8-bit horizontal) of the hit pixel and transmits the pixel address to the time-to-digital convertor (TDC) processor where it receives a 26-bit or greater time stamp and a two-bit quadrant address. The readout of 44-bit words that correspond to each photon event occurs continuously, with no dead time.

Operation of the address event-driven readout is conceptually simple; its timing is shown in Fig. 7. Following a threshold-crossing event from the discriminator of a pixel, the positive-edge-triggered digital logic located in the pixel initiates a read request, which is broadcast to the vertical and horizontal scanners. The vertical arbitration scanner re-times the pixel's event-driven request signal with that of the signaling from the other rows using a globally distributed scanner clock. The vertical arbitration scanner then polls the re-timed row requests and determines what row to read.

The vertical scanner cell has the logic necessary to process and capture pixel read requests. The vertical scanner input signal is a current that is provided by the pixels in the row. If no pixel in the row is hit, total current flowing into the vertical scanner input is zero. Each hit pixel provides a current of 30 μA to the vertical scanner, and, when multiple pixels in a row are hit, the current from all pixels is summed at the end of each row.

Inside the vertical scanner, the sum of pixel currents flows into a resistive transimpedance amplifier (RTIA) that converts the currents into an output voltage, signaling whether the row contains any hit pixels. The RTIA is implemented using a two-stage operational amplifier with a discriminator at the output, providing rail-to-rail digital signals. To avoid transition bounce at the output, there is hysteresis in the discriminator response, which makes the digital output signal less susceptible to noise.

The logic of the vertical arbitration scanners determines which row broadcast a photon-initiated event, by passing a token through the scanner. After polling the rows in the array, the vertical arbitration scanner selects a single row to read. The row-select signal then connects all of the pixels in that row to the horizontal scanner, and the logic of the horizontal scanner

is used to poll the pixels in the selected row to find the location of the pixel that was hit.

To ensure that no photon data is lost, when there are multiple pixel hits within the same scanner clock period, the tokens of the vertical scanner are first passed to the signaling row closest to the top of the quadrant. The pixel is addressed by the arbitration logic, and its event-driven logic is reset, eliminating its current contribution to the end-of-row RTIA. Pixels not read during the current vertical scanner clock period continue to contribute to the current flow into the end-of-row RTIA and are read in subsequent clock periods.

After the hit pixel is located, the vertical and horizontal arbitration scanners provide the x and y pixel address (8 bits for each x and y address) of the photon event. Since the pixels perform discrimination, i.e., detecting only whether the pixel was hit or not, the readout from the sensor is purely digital, and therefore is noiseless. After providing this output address data, the horizontal scanner clears the pixel that was read, preparing the pixel to detect subsequent X-ray photon events.

Because the EDATS-XPC sensor design can only output a single pixel address every scanner clock period (a necessary limitation enforced by scanner polling), the maximum number of events that can be processed by each quadrant of the VX-807 ROIC is equal to the scanner clock frequency, which is nominally about 25 MHz. There are several settling times that ultimately determine the maximum clock rate, and the corresponding maximum event readout speed. These time delays include pixel row request settling time, vertical scanner polling time, column event settling time, and horizontal scanner polling time. The longest token propagation time is a scanner clock period that is twice the column event timing plus the time of the horizontal scanner polling, where it is assumed that the scanner clock has a 50% duty cycle and that the vertical and horizontal scanners use a similar token propagation scheme.

The maximum readout speed also depends upon the spatial/temporal distribution of the X-ray photon events. From a system perspective, these factors combine to limit the maximum X-ray flux rates that can be handled by the EDATS detector. As a result, to decrease token-propagation time (polling time) and increase count-rate capabilities of the VX-807 ROIC, we partitioned the token-propagation circuits into 16 subscanning circuit blocks, each configured with 32 token propagation elements.

Simulations of EDATS operation show, in each quadrant, a nominal horizontal and vertical scanner polling time of about 9.2 ns, with a worst case scanning time of 11.2 ns, which was calculated by assuming CMOS processing conditions that resulted in the largest magnitude of delay times. For the 11.2 ns (worst case) polling times, with a clock delay time of 2.5 ns (resulting from the lag in the distribution of the scanner clock across all four quadrants of the array) and with a column-event settling time of 7 ns, the worst case output address rate in each quadrant is 23.8 MHz (42 ns jitter). With nominal CMOS processing conditions, it is expected that a 25 MHz rate will be achieved in each quadrant, allowing the EDATS detector to operate with a global 100 MHz X-ray photon count rate.

4) Pixel Enable (Disable) Circuits: Because of the normal variations in the size of the transistor and passive components

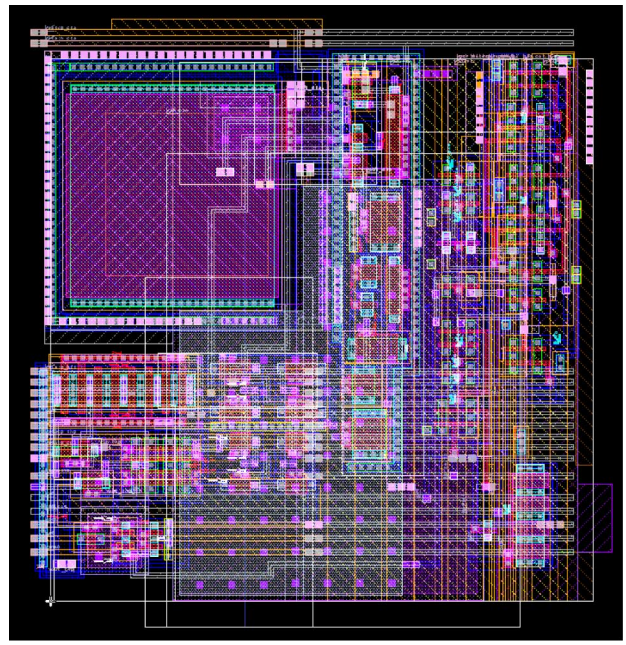

Fig. 8. Layout of 40-μm pitch EDATS-XPC sensor pixel. The analog and pad portion of the pixel requires $\sim 73\%$ of the pixel and the remaining 27% is used by the digital broadcast logic.

across the array, the gain of each CTIA, the noise of the AFE, and the offset of the comparators in each pixel can be expected to be different across the array. Due to process variations distributed across the array, statistically, outlying *bad* pixels may result. These bad pixels can cause excessive triggering of the comparator, and, thus, must be minimized. Otherwise, those pixels that have high false-event triggering would request access to the readout bus excessively, which could prevent properly functioning pixels from access. Assuming that a discriminator threshold is set at a value 3σ larger than the average system noise level, σ, even with ideal processing conditions, statistically, at least one bad pixel per array must be powered down. In practice, depending on the detector array and CMOS processing characteristics, more pixels are generally disabled so as to allow optimal detector performance. The VX-807 ROIC powers down pixels using control signals supplied by the vertical scanner.

5) Pixel Layout: The layout of pixel circuits is shown in Fig. 8. The analog and pad portion of the pixel requires $\sim 73\%$ of the pixel and the remaining 27% is used by the digital broadcast logic.

C. Silicon Photodiode Array

1) Photodiode Design and Fabrication: Using the Silvaco ATLAS device and ATHENA process simulator tools, 40-μm-pitch PIN photodiodes were designed for fully depleted operation when implemented in 20-μm-thick silicon. Device simulations verify the dopant implant and anneal schedules of the design through verification of key performance parameters including: full device depletion at a low detector bias voltage, low capacitance, proper pixel-to-pixel anode isolation, and reduction of surface electric fields for reduced dark current generation. Fig. 9 shows the simulated 2D potential profile

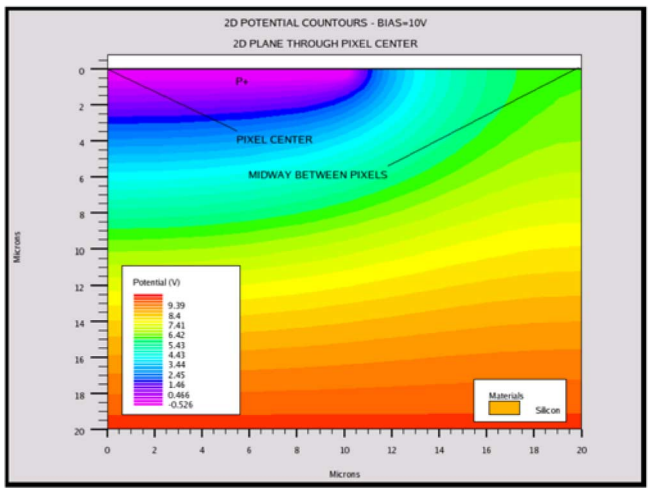

Fig. 9. Simulated 2D potential profile for the photodiode design with 40-μm pixel pitch and 20-μm p+ anode implant. The simulation shown is with 10 V reverse bias across the device.

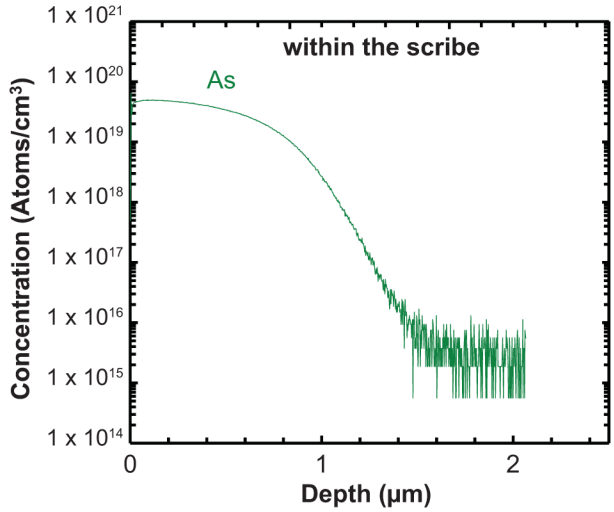

Fig. 10. SIMS data of the n+ implant measured at the X-ray incident surface of the detector.

for a 40-μm pitch photodiode design with a 20-μm p+ anode implant, operated at a 10 V reverse bias.

Fully depleted 492×492 pin photodiode arrays were fabricated on custom 6-in silicon-on-insulator (SOI) wafers, with a 20-μm-thick, 4000 Ω-cm float zone silicon (n-), silicon layer on top of a 1-μm-thick buried oxide (BOX) and a 650-μm-thick handle wafer.

The p+ anodes of the photodiodes were formed by implanting dopants into the front of the wafer. The common cathode contact to the array was made on the back of the device, with a global heavy n+ implant introduced into the bottom of the active SOI layer during wafer assembly at Isonics, Inc., Vancouver, WA, USA. Simulations show that the fully depleted photodiodes have a capacitance of 6.0 fF.

Following fabrication, the wafers were tested using an automated wafer probe station. *I–V* measurements indicate very good detector array yields and uniform photodetector performance across the wafer. *C–V* measurements show that the detector approaches full depletion at a reverse bias of approximately 5 V. Fig. 10 shows measured secondary ion mass spectroscopy (SIMS) of the detector's heavily n+ implanted back surface, showing the good implant shape required to minimize dead-space effects.

After screening, diced and individual arrays were packaged in chip carriers for electrical and optical lab evaluation. Candidate devices were then hybridized to the VX-807 ROIC using flip-chip solder bumping, performed using a SET-150 die bonder.

D. Time Stamping and Correlation Processing

To allow real-time spatial and temporal correlation of X-ray photon events, each quadrant of the VX-807 ROIC used in the EDATS-XPC detector is designed to interface with Voxtel's VX-567 model (or equivalent) TDC processor. The VX-567 TDC is based on a field-programmable gate array (FPGA) architecture, wherein up to 512 parallel inputs can be time-stamped simultaneously to better than 50-ps accuracy, at rates up to 300 MHz in each channel. The VX-567 TDC is also capable of performing real-time auto- and cross-correlation processing across multiple channels. For example, autocorrelation with 3-ns delay times can be performed over eight channels simultaneously.

Early calculation of the correlation coefficients reduces the amount of data that needs to be transmitted through the system. For the four-quadrant outputs of the 242 064 element EDATS-XPC array, which requires only 1-μs time delay, the autocorrelation of OR-logic sum regions of interest of greater than 1024 speckles can be processed in real time. Alternatively, the VX-567 TDC can be configured to buffer each 32-bit time stamp, along with the 18-bit pixel address (8-bit x address, 8-bit y address, and 2-bit quadrant address), before transmitting the 44-bit time-stamped address, via a gigabit Ethernet interface, for processing in the host computer.

III. XPC Pixelated Array Detector Test and Verification

After verifying the general operation of hybridized EDATS sensor chip assemblies, the integrated test pixel, located in the top row of quadrant three (upper right corner) in the VX-807 ROIC, were used to characterize the conversion gain of the pixel circuits. The test pixel is similar to the other pixels in the array; however, it features a charge injection circuit that allows for the injection of a controlled electrical charge into the pixel, without the need for a detector array, as well as analog test points of the outputs of the AFE circuits and the discriminator stages.

A. Pixel Circuit Conversion Gain Measurements

To determine the conversion gain of the AFE circuits, a fixed amount of charge was input to the pixel. The resultant pulse height was measured at the output of the AFE. This pulse height was then used to calculate the conversion gain of pixel AFE circuits. These conversion gain measurements are labeled "Meas2" in Fig. 11. Next, for a fixed shaper feedback resistance, a fixed amount of charge was input to the pixel, and the threshold voltage level at which the pixel triggers on 50% of the input pulses was used to determine the conversion gain. These data are labeled "Meas1" in Fig. 11. As seen in the figure,

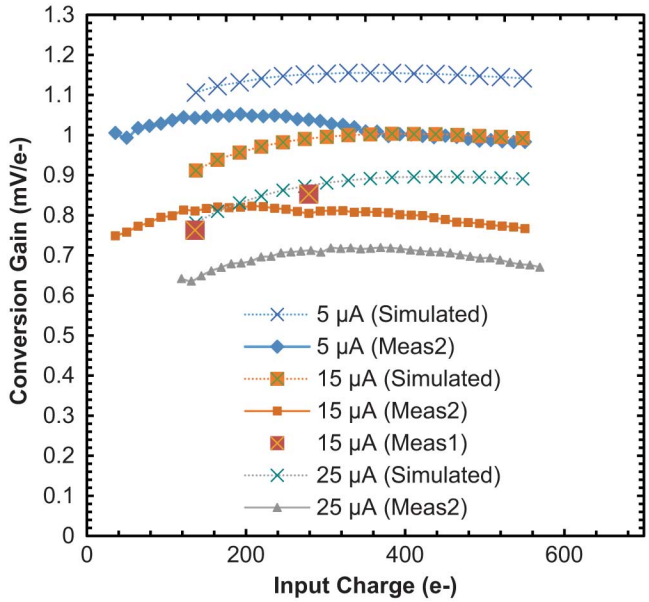

Fig. 11. Comparison of measured versus simulated VX-807 ROIC pixel conversion gains for several different shaper feedback resistances. This measurement was taken using the ROIC test pixel and charge injection circuit.

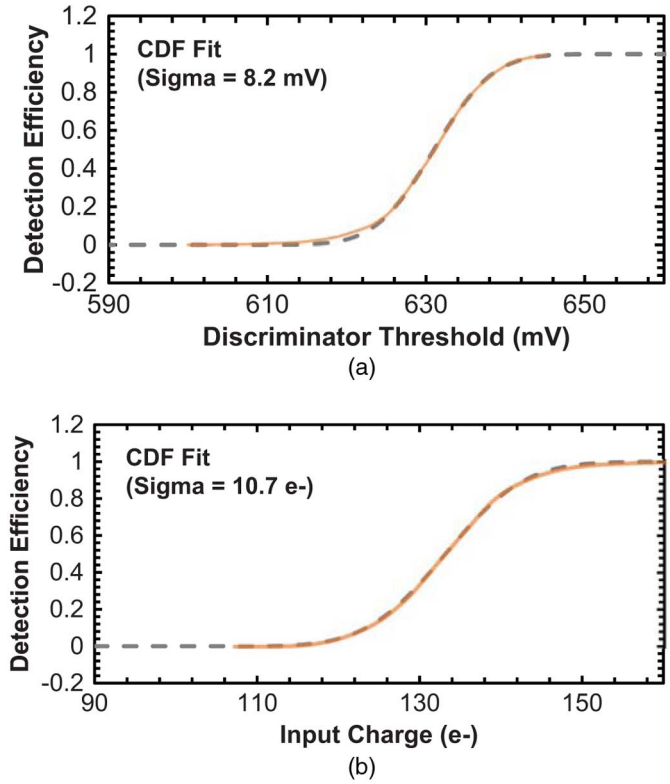

Fig. 12. Electrical noise measurements of the VX-807 ROIC pixel using an electrical charge injection circuit (500 eV equivalent input). The noise is measured to be about 11 e^- by sweeping both the discriminator threshold (top) and the input charge (bottom). Note that in the top figure, the threshold levels are absolute offset values referenced from highest reference voltage level.

both measurement techniques result in a similar conversion gain for the pixel design.

B. Pixel Noise Measurements

Measurement of EDATS-XPC sensor pixel noise was conducted by injecting a charge pulse approximately six-times greater than the expected noise floor of the pixel, and measuring the count rate at various comparator threshold voltage levels. At each threshold voltage level, 256 charge pulses were captured using an oscilloscope and averaged. These results are plotted in Fig. 12, top, which shows measured detection efficiency as a function of discriminator threshold. Generally, the faster the rate at which the detection efficiency transfers from 0% to 100%, the lower the noise level of the pixel. Comparing an ideal cumulative distribution function (CDF) of a Gaussian distribution to the measured transfer curve reveals a pixel circuit noise of 8.2 mV RMS.

In a second noise measurement, the discriminator threshold was held at a set voltage level, and the amount of charge injected into the circuit was varied. The fit of the CDF for these measurements reveals a circuit noise of 10.7 e^- RMS (see Fig. 12, bottom), less than the 15.5 e^- RMS value simulated, but well within the limits of the assumptions of the experiment and the measurement accuracy. Dividing the RMS discriminator noise by the RMS input noise, reveals a conversion gain of 762 μV/e^-; this value is close to the measured conversion gain reported above. Converting the noise measurements to equivalent photon energy results in an X-ray photon energy noise of 39 eV RMS.

C. Tests Under Optical Illumination

Following completion of device hybridization, optical characterization of the EDATS sensor was completed.

Sensor response to fast laser pulses was measured at the output test node of the AFE. As shown in Fig. 13, the output of the AFE is a pulse that, compared with the delta-like input current pulse, is band-limited. By varying the feedback resistance of the shaper stage, gate voltage on the R_{INT} FET is modulated. As a result, a change in gain and pulse width of the AFE output is able to be measured. As can be seen in Fig. 13, at higher shaper feedback resistances (lower external bias current), the AFE output pulse height is higher, but the AFE output pulse is also longer, resulting in a potential minimum interpulse time of several microseconds. At the lower feedback resistance (high external bias current), the AFE output pulse height is reduced, but the potential interpulse interval is about 2.0 μs. Little change is seen in the measured conversion gain of the hybridized sensor in comparison to the previously described electrical conversion gain.

In this mode, the sensor was verified to count correctly the individual pulses from the laser source. Verification was attained by triggering the laser driver with a known number of electrical pulses (i.e., 100) and observing that the same number of counts were detected by the array. This was repeated at several locations across the array, and no dead pixels were observed during lab measurements of two hybridized devices.

1) Photon Detection Efficiency and Dark Count Rates: First, the sensor discriminator threshold levels required to detect a given input charge pulse were measured. The threshold levels at which the pixels successfully detected 50% of the input pulses

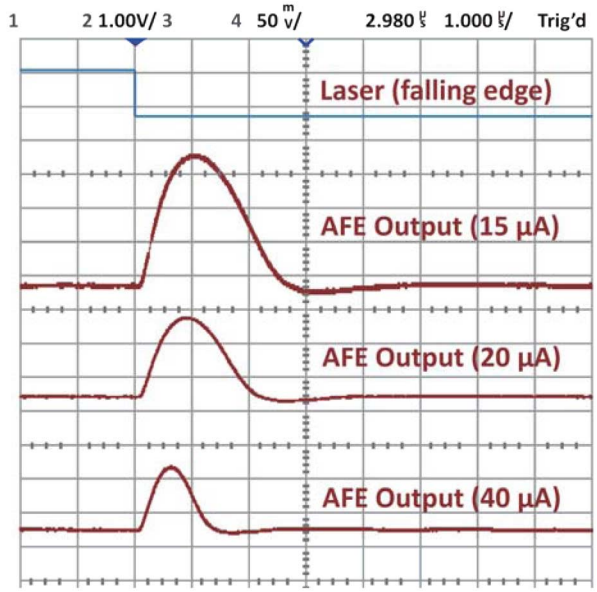

Fig. 13. Measurements showing the band-limited AFE output after injection of a 100-ps optical signal. The AFE outputs shown were obtained by varying the feedback resistance of the shaper stage, the change in gain, and pulse-pair resolution of the pixel AFE.

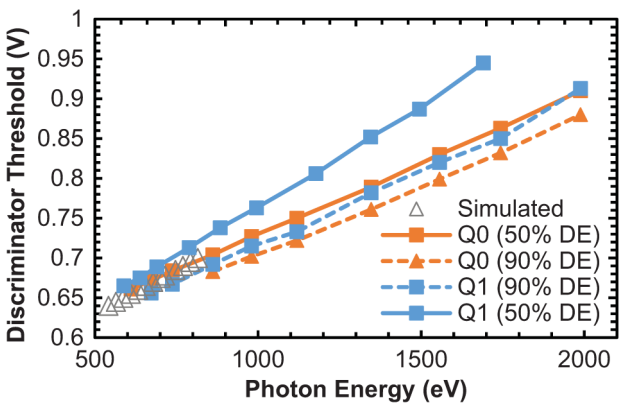

Fig. 14. Measured discriminator threshold level required to detect the photons of a given energy (shown for 50% and 90% detection efficiency, DE). The sensor response is linear over the range 0.5 to 2.0 keV.

were recorded. As seen in Fig. 14, the relationship between the input photon energy and the required discriminator threshold is linear over the target range of 500 eV to 2.0 keV X-ray photons. For 2.0 keV X-ray photons, it is assumed that the nominal photon-to-electron hole conversion in the silicon detector is 3.65 eV/e^-, which allows for a threshold-to-photon energy conversion of 200 μV/eV to be determined.

To characterize the dark count rate (DCR) of the sensor, the optical illumination of the sensor was turned off, and the number of dark counts were recorded as a function of the discriminator threshold level. These threshold levels were then mapped to an equivalent X-ray photon energy using the threshold versus input energy ratio data in Fig. 14.

Based on our modeling of the EDATS sensor, it was anticipated that false counts would originate from the fixed pattern noise that results from the gain variations and discriminator offset values of the AFE circuits. For this reason, the VX-807 ROIC is designed such that individual rows within the design that contain bad pixel elements can be turned off to lower the overall DCR of the sensor.

The data in Fig. 15 show how disabling rows of the sensor can be used to reduce the dark count rate of the EDATS-XPC detector by an order of magnitude or more. As expected, the dark count drops quickly as the X-ray energy threshold increases—approximately an order of magnitude every 125 eV of detection level. At the 500 eV and 1.0 keV detection levels, the DCR is measured to be 1×10^3 counts/s/quadrant and 10 counts/s/quadrant, respectively.

The timing jitter of the EDATS detector is determined by: 1) the minimum time that it takes the arbitration scanners to identify and clear the pixel that has detected a photon hit; and 2) the timing jitter that results from the pixel AFE bandwidth and noise limitations. The speed of the address arbitration scanners is limited by the token propagation and the external arbitration clock, which must be set to a sufficiently low frequency so that there are no timing violations within the arbitration scanners resulting from settling times. Based on simulation, the arbitration clock could run up to 24 MHz. However, in the test camera, the master clock was limited to about 15.625 MHz, resulting in a minimum measurable time resolution of 64 ns and a maximum allowable photon rate across the array of 62.5 MHz.

To characterize the operation of the arbitration scanners, 1000 digital test pulses were injected into a single pixel at rates from 1 to 100 kHz. The measured time stamps had an 81.4 ns RMS jitter. To characterize the overall timing jitter of the EDATS detector, including both arbitration and pixel noise sources, pixels were illuminated by laser pulses of a magnitude equivalent to a 1.0 keV photon energy, at various repetition rates (e.g., 1, 10, 50, and 100 kHz). The comparator threshold voltage levels were set to achieve a dark count rate of approximately 45 dark counts/s.

Fig. 2 shows the time stamp precision measured from 1000 laser pulses delivered at a 1 kHz repetition rate. The jitter was measured to be 81.4 ns RMS. As the input signal repetition rate was increased from 1 to 100 kHz, a slight degradation of the timing resolution was observed. At 1, 10, 50, and 100 kHz input to a single pixel, the measured photon detection efficiencies were found to be 99.9%, 99.8%, 99.7%, and 90.4%, respectively. We believe both the degradation to the photon detection efficiency and the increase in the timing jitter to be due to saturation of the AFE CTIA. In a CTIA, the amplifier input is reset using the feedback to the input, and, when the event rate exceeds the reset rate, the input is not completely restored. As the CTIA saturates, the pulses at its output are reduced in amplitude, which, given a fixed comparator threshold, can result in increased noise and missed photon events.

IV. Conclusion

An event-driven pixelated X-ray detector architecture capable of photon counting at 100 MHz rates, with better than 85 ns time stamping was designed, and its performance was shown to match the simulated performance and to be compatible to the requirements for XPCS experiments. The asynchronous, event-driven architecture eliminates dead time and reduces the data bandwidth compared with framing area cameras and improves the SNR of speckle imaging. Further reductions in

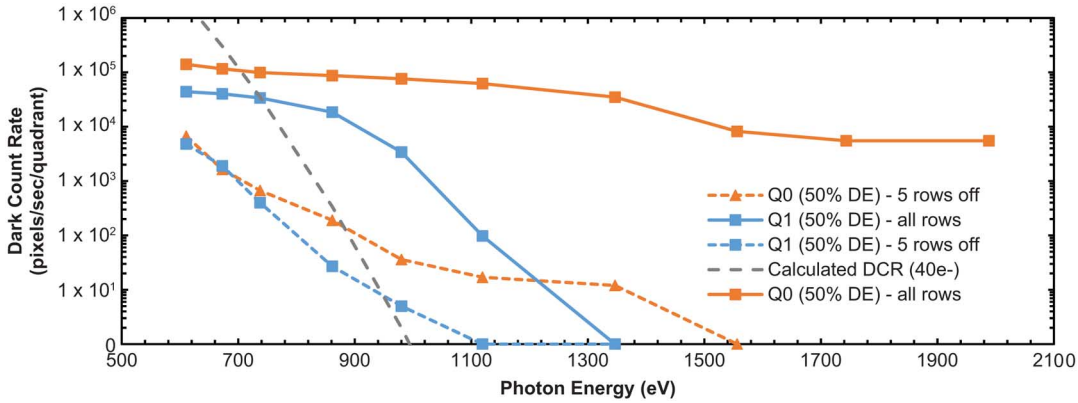

Fig. 15. Dark count rate (DCR) of sensor before and after disabling five rows in each quadrant. The dark count drops quickly as the X-ray energy threshold is increased. As an approximation, the DCR of the EDATS-XPC sensor drops by an order of magnitude every 125 eV.

the timing jitter can be achieved by increasing the bandwidth of the AFE circuits and by increasing the number of arbitration circuits from the four used in the current design.

ACKNOWLEDGMENT

The authors would like to thank the DOE Program Manager L. Wilson.

REFERENCES

[1] M. S. Pierce *et al.*, "Quasistatic Xray speckle metrology of microscopic magnetic return-point memory," *Phys. Rev. Lett.*, vol. 90, no. 17, p. 175502, Apr. 2003.
[2] M. Sutton *et al.*, "Observation of speckle by diffraction with coherent Xrays," *Nature*, vol. 352, no. 6336, pp. 608–610, Aug. 1991.
[3] A. C. Price *et al.*, "Coherent soft-xray dynamic light scattering from smectic-A films," *Phys. Rev. Lett.*, vol. 82, no. 4, p. 755, Jan. 1999.
[4] S. G. J. Mochrie *et al.*, "Dynamics of block copolymer micelles revealed by X-ray intensity fluctuation spectroscopy," *Phys. Rev. Lett.*, vol. 78, no. 7, pp. 1275–1278, Feb. 1997.
[5] B. Hu *et al.*, "Coherent soft Xray magnetic scattering," *Synchrotron Radiat. News*, vol. 14, no. 2, pp. 11–19, Mar. 2001.
[6] Z. H. Cai *et al.*, "Observation of Xray speckle by coherent scattering at grazing incidence," *Phys. Rev. Lett.*, vol. 73, no. 82, Jul. 1994.
[7] S. Brauer *et al.*, "Xray intensity fluctuation spectroscopy observations of critical dynamics in Fe3Al," *Phys. Rev. Lett.*, vol. 74, no. 11, pp. 2010–2013, Mar. 1995.
[8] S. B. Dierker *et al.*, "Xray photon correlation spectroscopy study of Brownian motion of gold colloids in glycerol," *Phys. Rev. Lett.*, vol. 75, no. 3, p. 449, Jul. 1995.
[9] I. A. Vartanyants and I. K. Robinson, "Partial coherence effects on the imaging of small crystals using coherent X-ray diffraction," *J. Phys. Condens. Matter*, vol. 13, no. 47, p. 10593, Nov. 2001.
[10] U. Weierstall *et al.*, "Image reconstruction from electron and X-ray diffraction patterns using iterative algorithms: Experiment and simulation," *Ultramicroscopy*, vol. 90, no. 2–3, p. 171, Feb. 2002.
[11] J. Miao and D. Sayre, "On possible extensions of X-ray crystallography through diffraction-pattern oversampling," *Acta Crystallogr. A Found. Crystallogr.*, vol. 56, no. 6, pp. 596–605, Nov. 2000.
[12] T. Thurn-Albrecht *et al.*, "Photon correlation spectroscopy of colloidal palladium using a coherent X-ray beam," *Phys. Rev. Lett.*, vol. 77, no. 27, p. 5437, Dec. 1996.
[13] P. Falus, M. A. Borthwick, and S. G. J. Mochrie, "Fast CCD camera for xray photon correlation spectroscopy and time-resolved X-ray scattering and imaging," *Rev. Sci. Instrum.*, vol. 75, no. 11, pp. 4383–4400, Nov. 2004.
[14] A. P. Y. Wong and P. Wilzius, "Dynamic light scattering with a CCD camera," *Rev. Sci. Instrum.*, vol. 64, no. 9, pp. 2547–2549, Sep. 1993.
[15] E. Jakeman, "Photon correlation," in *Photon Correlation and Light Beating Spectroscopy*, ser. NATO Advanced Study Institutes Series, Series B: Physics, H. Z. Cummins and E. R. Pike, Eds. Boston, MA, USA: Springer, 1974, vol. 3, ch. 4, pp. 75–149.
[16] N. A. van Bakel *et al.*, "Timepix detector at the X-ray correlation spectroscopy instrument at LCLS," *J. Phys. Conf. Ser.*, vol. 425, no. 6, p. 062011, Mar. 2013, 10.1088/1742-6596/425/6/062011, IOP Publishing.
[17] C. Ponchut *et al.*, "MAXIPIX, a fast readout photon-counting X-ray area detector for synchrotron applications," *J. Inst.*, vol. 6, no. 1, p. C01069, Jan. 2011, 10.1088/1748-0221/6/01/C01069, IOP Publishing.
[18] C. Granja *et al.*, "Spatially correlated and coincidence detection of fission fragments with the pixel detector timepix," *IEEE Nucl. Sci. Symp. Conf. Rec.*, pp. 1578–1584, Oct. 2010, 10.1109/NSSMIC.2010.5874042.
[19] T. Hoshino, M. Kikuchi, and D. Murakami, "X-ray photon correlation spectroscopy using a fast pixel array detector with a grid mask resolution enhancer," *J. Synchrotron Rad.*, vol. 19, no. 6, pp. 988–993, Nov. 2012.